Nano Research

Open Access

Research Article

Silicon-based metal-organic frameworks (SiMOFs) for immunogenic cell death in cancer therapy

Min Han[1], Zishan Chen[1], Shiying Zhou[1], Zunde Liao[1], Xiangting Yi[1], Yao He[3] ✉, Yiling Zhong[1] ✉, and Kam W. Leong[2] ✉

[1] *College of Pharmacy, State Key Laboratory of Bioactive Molecules and Druggability Assessment, Jinan University, Guangzhou 511443, China*
[2] *Department of Biomedical Engineering, Columbia University, New York, NY 10027, USA*
[3] *Institute of Functional Nano and Soft Materials (FUNSOM), Soochow University, Suzhou 215123, China*

Cite this article: *Nano Research*, **2025**, *18*, 94907080. https://doi.org/10.26599/NR.2025.94907080

ABSTRACT: Silicon-based nanomaterials, known for their unique properties and favorable biocompatibility, significantly impact sectors like energy, electronics, and biomedicine. Recently, metal-organic frameworks (MOFs) have emerged as promising candidates for biomedicine, characterized by adjustable chemical composition, high porosity, and biodegradability. However, the combination of silicon with MOFs to create silicon-based MOF nanostructures (SiMOFs) remains underexplored. Herein, we establish a diverse library of SiMOFs with various nanostructures, including flower-like, capsule-like, hexagonal snowflake-like, and necklace-like morphologies via microwave-assisted synthesis. These SiMOFs, with their spacious interiors, are ideal for drug delivery. They are used to load drugs and create drug-loaded SiMOFs (e.g., SiFeO). SiFeO exhibits excellent photothermal effects and high reactive oxygen species (ROS) generation capacity, enabling synergistic treatments involving chemo-chemodynamic-photothermal therapy. This approach efficiently triggers immunogenic cell death (ICD) and demonstrates excellent antitumor efficacy *in vivo*. Immunofluorescence staining reveals that the synergistic therapy can modulate the tumor microenvironment (TME) by reducing M2-phenotype macrophages, increasing the activation of antigen-presenting cells (APCs), enhancing the infiltration of $CD4^+$ and $CD8^+$ T cells, elevating Granzyme B production, and decreasing the presence of immunosuppressive regulatory T cells (Tregs). Consequently, drug-loaded SiMOFs-mediated combination therapy effectively reverses the immunosuppressive TME and activates robust antitumor immune responses by inducing ICD in tumor cells, ultimately achieving superior anticancer efficacy.

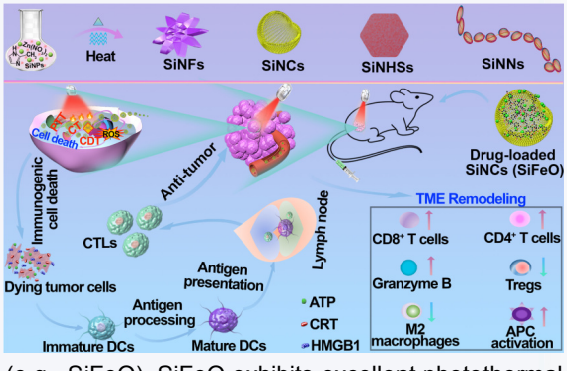

KEYWORDS: silicon-based nanomaterials, nanocarriers, immunogenic cell death, antitumor immune responses

1 Introduction

Functional silicon-based nanomaterials, known for their biocompatibility, unique optical/electronic properties, and surface tailorability, have garnered significant scientific interest [1–3]. In recent years, there has been noteworthy progress in the fabrication of silicon-based nanomaterials, including silicon nanoparticles, silicon nanowires, and mesoporous silica nanoparticles [4–10]. The structural morphology of these nanomaterials plays a crucial role in defining their surface and chemical properties, tailoring them for various applications [11]. For instance, silicon nanoparticles are used in bioimaging due to their controllable optical properties and small size [4, 5, 12, 13]. Silicon nanowires, with their rapid response and facile surface modification, are attractive for electrochemical and optical biosensors for sensitive detection of biological targets like DNA and proteins [14, 15]. Mesoporous silica nanoparticles, known for their high surface area and ordered porous network, are excellent for drug delivery applications [9, 16–18]. This motivates us to further explore other features and applications of silicon-based nanomaterials.

Metal-organic frameworks (MOFs), offering functional porous materials with unique properties, have emerged as a promising

Received: July 6, 2024; **Revised:** October 14, 2024
Accepted: October 17, 2024

✉Address correspondence to Yao He, yaohe@suda.edu.cn; Yiling Zhong, zhongyiling5866@gmail.com; Kam W. Leong, kam.leong@columbia.edu

candidate in biomedicine, surpassing traditional materials like silica and zeolites in versatility [19, 20]. However, silicon-based MOF nanostructures remain underexplored. We hypothesize that silicon-based MOF nanostructures, combining the advantages of silicon and MOF structures, may hold significant promise in drug delivery applications, and we proceed to test the hypothesis in cancer immunotherapy.

Cancer continues to be a leading cause of disease-related death [21–25]. Inducing immunogenic cell death (ICD) in cancer cells, characterized by the release of damage-associated molecular patterns (DAMPs) and proinflammatory cytokines, is a promising strategy for cancer therapy [26–29]. This approach, which can transform immunosuppressive tumors into immunogenic ones, relies on DAMPs like calreticulin (CRT) and adenosine triphosphate (ATP) to activate immune responses against cancer [29]. Recent advances in nanodrug-based treatments, such as radiotherapy, chemotherapy, chemodynamic therapy, and photothermal therapy, have shown potential in triggering ICD in tumor cells [30–34]. Despite such progress, continued research in creating multifunctional nanodrugs with strong ICD-inducing activity remains a crucial and worthwhile area of pursuit [35–44].

Herein, we reported the microwave-assisted synthesis of silicon-based MOF nanostructures (SiMOFs) with diverse morphologies, including flower-like, capsule-like, hexagonal snowflake-like, and necklace-like structures, by altering reaction agent ratios (Scheme 1(a)). These SiMOFs, due to their large interior spaces and specific surface areas, were excellent nanocarriers for drug delivery. Considering the advantages of curcumin as a natural chemotherapeutic agent in cancer therapy [45–47], we specifically used capsule-like SiMOFs (SiNCs) to load curcumin, forming SiNCs@Curcumin. This composite was further reacted with Prussian blue to produce iron-based nanoparticles on SiNCs, creating SiFeO (curcumin and iron-based nanoparticles decorated SiNCs) nanocomposites. Numerous studies have demonstrated that iron-based nanomaterials possess unique properties and multifunctional capabilities, making them promising candidates for

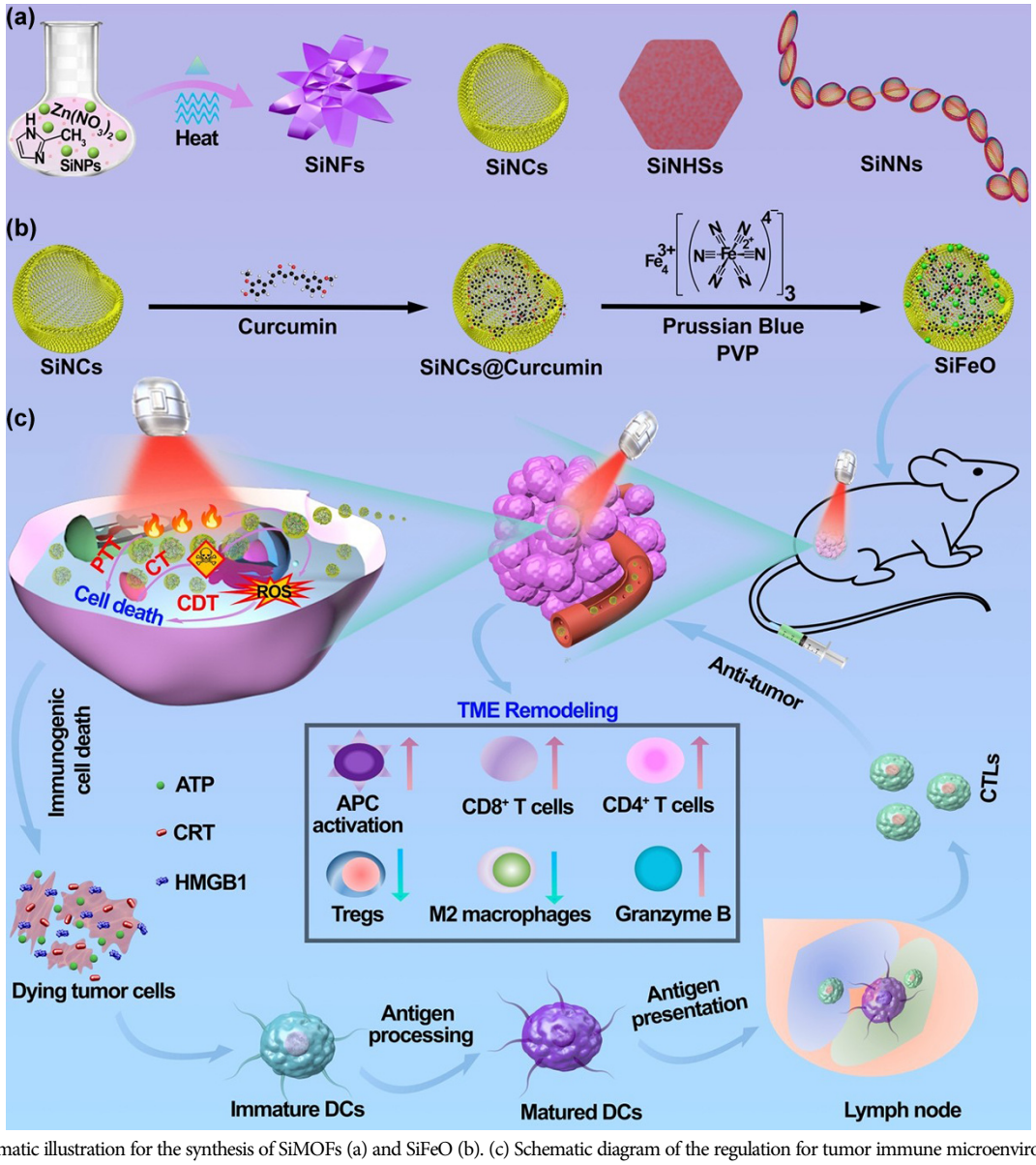

Scheme 1 Schematic illustration for the synthesis of SiMOFs (a) and SiFeO (b). (c) Schematic diagram of the regulation for tumor immune microenvironment to inhibit breast cancer tumor.

combination therapies such as photothermal and chemodynamic therapy [48, 49]. Photothermal and chemodynamic therapies are promising cancer treatments that employ distinct mechanisms to selectively destroy cancer cells while minimizing damage to surrounding healthy tissues [50, 51]. Photothermal therapy uses light-absorbing agents to convert light into heat, creating localized hyperthermia that kills tumor cells [52]. In contrast, chemodynamic therapy utilizes catalytic agents to produce reactive oxygen species (ROS) within tumors, causing oxidative stress that leads to cancer cell death. As anticipated, SiFeO exhibited a strong photothermal effect and ROS generation ability, achieving synergistic chemo-chemodynamic therapy-photothermal (CT-CDT-PTT) cancer therapy. This combined therapeutic approach effectively induced ICD in tumor cells, thereby enhancing their immunogenicity. This increased immunogenicity facilitated the recruitment of tumor-infiltrating cytotoxic T lymphocytes (CTLs), significantly boosting the anticancer efficacy of the treatment (Scheme 1). In a 4T1 breast cancer murine model, the SiFeO-mediated CT-CDT-PTT combination therapy effectively eliminated the tumors with minimal collateral damage to normal tissues, demonstrating the potential of SiFeO as an effective nanodrug for cancer therapy.

2 Experimental

2.1 Synthesis of SiNPs

Firstly, original silicon nanoparticles (O-SiNPs) were prepared according to our previous report [6]. Briefly, 100 mL of (3-aminopropyl)trimethoxysilane was added to 400 mL of an aqueous solution containing 0.1 g of fluorescein sodium and stirred for 20 min to ensure thorough mixing. The mixture was then transferred into a 30 mL vitreous vessel for a one-pot microwave reaction at 180 °C for 60 min. After microwave irradiation, the solution was allowed to cool naturally to room temperature. Subsequently, the solution was purified by dialysis (MWCO: 500, Viskase) to obtain O-SiNPs. The as-prepared O-SiNPs were further modified with glyoxylic acid. In short, 300 mg of glyoxylic acid was added to a solution containing 60 mL of O-SiNPs and 20 mL of acetic acid, and the mixture was stirred at room temperature for approximately 180 min. Subsequently, the pH of the mixture was adjusted to around 4.5 using NaOH solution and stirred for an additional hour. Then, 110 mg of sodium borohydride was introduced, and the mixture was stirred for another 2 h to produce the modified O-SiNPs (referred to as SiNPs). To isolate residual reagents, 2-propanol was added dropwise to the SiNPs solution until it became slightly turbid, followed by centrifugation. The purified SiNPs precipitates were then re-dispersed in water.

2.2 Synthesis of SiMOFs

The obtained SiNPs were added to an aqueous solution containing zinc nitrate and 2-methylimidazole with continuous stirring. After thorough mixing, the solution was injected into a 30 mL glass vessel for a microwave reaction at 120 °C for 3 h. SiMOFs with varied morphologies were obtained by adjusting the mass ratio of SiNPs/zinc nitrate/2-methylimidazole. Typically, flower-like SiMOFs (SiNFs), capsule-like SiMOFs (SiNCs), and necklace-like SiMOFs (SiNNs) were respectively obtained under the following conditions (mass ratios of SiNPs/zinc nitrate/2-methylimidazole): 5.5:1:6.3, 3.4:1:6.3, and 2.8:1:6.3. Interestingly, when an appropriate amount of PEG was added to the precursor solution with a 5.5:1:6.3 mass ratio of SiNPs/zinc nitrate/2-methylimidazole (e.g., setting the mass ratio of SiNPs/zinc nitrate/2-methylimidazole/PEG to 5.5:1:6.3:0.8), hexagonal snow-like SiMOFs were produced after the microwave reaction at 120 °C for 3 h. After microwave irradiation, the solution containing SiMOFs was allowed to cool naturally to below 30 °C, and then further purified by centrifugation to isolate the SiMOFs.

2.3 Preparation of SiFeO

10 mL of a SiNCs aqueous solution (3 mg/mL) was added dropwise into 60 mL of methanol containing 100 mg of curcumin under stirring. The resulting mixture was stirred at room temperature for 24 h. Subsequently, the mixture was centrifuged and washed with methanol and water to obtain purified SiNCs@Curcumin. Subsequently, 5 mL of 2 mg/mL Prussian blue aqueous solution was added to the SiNCs@Curcumin aqueous solution, followed by 24 h of stirring under ambient conditions. The mixture was centrifuged to collect the green precipitate (SiFeO), which was washed with water twice. The green precipitate was redispersed in water, and polyvinylpyrrolidone (PVP) was introduced to the solution under stirring at ambient temperature. After stirring for 24 h, the mixture containing SiFeO was collected and purified by centrifugation and washing with water, resulting in SiFeO with excellent water dispersibility. For the preparation of iron-based nanoparticles (CPB), 5 mL of a Prussian blue aqueous solution (2 mg/mL) was added to the curcumin aqueous solution and stirred at room temperature for 24 h. The mixture was then centrifuged to obtain the CPB precipitate, which was subsequently washed with water twice. Subsequently, a PVP aqueous solution was added to the water solution containing CPB and stirred for 24 h. Finally, the mixture was purified to obtain the as-prepared CPB.

SiFeO nanoparticles were suspended in ultrapure water to prepare a homogenous dispersion. The hydrodynamic diameter of the nanoparticles was measured at specified time intervals using dynamic light scattering (DLS) to monitor any changes in particle size over time. Measurements were conducted at multiple time points to construct a stability curve ($n = 3$).

Hemolysis assay of SiFeO: Fresh blood was collected from healthy BALB/c mice and centrifuged at 2000 rpm for 5 min to separate red blood cells (RBCs). The isolated RBCs were then washed three times with phosphate buffer saline (PBS) and resuspended in PBS. The suspension was diluted to achieve a final RBC concentration of 2% (v/v). Next, 200 μL of the 2% RBC suspension was mixed with 200 μL of SiFeO at various concentrations. The mixtures were incubated at 37 °C for 4 h. PBS served as the negative control (indicating no hemolysis), while ultrapure water was used as the positive control (indicating complete hemolysis). After incubation, the samples were centrifuged at 10,000 rpm for 10 min, and the supernatants were carefully collected. The absorbance of the supernatants was measured at 540 nm using a microplate reader. The hemolysis rate was calculated using the following formula: Hemolysis rate (%) = $(OD_{sample} - OD_{negative\ control})/(OD_{positive\ control} - OD_{negative\ control}) \times 100\%$. All experiments were performed in triplicate ($n = 3$) to ensure accuracy and reproducibility.

2.4 Hydroxyl radicals (·OH) generation ability

The generation of ·OH was examined using ultraviolet–visible (UV–Vis) spectroscopy. In brief, a solution containing 0.2 mM 3,3' 5,5'-tetramethyl-benzidine (TMB) was treated with various

formulations and incubated at room temperature for 1 h under both pH 7 and pH 5.5 conditions. The ·OH-induced oxidation of TMB was monitored by measuring the changes in absorbance intensity at 652 nm.

2.5 Photothermal performance assessment

The impact of CPB/SiFeO concentration on the photothermal effect was investigated using different concentrations of CPB/SiFeO under identical laser radiation conditions (808 nm, 1 W/cm^2, 20 min). Additionally, a 100 μg/mL CPB/SiFeO aqueous solution was irradiated with an 808 nm laser at various power densities to assess the influence of power density on the photothermal effect. The photostability of CPB/SiFeO was also evaluated. In this experiment, a 100 μg/mL CPB/SiFeO aqueous solution was irradiated with an 808 nm laser at 1 W/cm^2 for 5 min, followed by turning off the NIR laser and allowing the solution to cool naturally for 15 min. This cycle was repeated four times to assess photostability.

2.6 Cellular uptake study

To assess the cellular uptake of SiFeO, 4T1 cells were seeded in plates and incubated overnight. Subsequently, the 4T1 cells were exposed to Cy7-labeled SiFeO for 6 h in a humidified incubator with 5% CO_2 at 37 °C. After the treatment, the following steps were performed: (1) The cells were washed twice with PBS and reincubated in a fresh medium containing LysoTracker Green for 1 h. Following this, the cells were stained with Hoechst 33342 for approximately 30 min. After two additional washes with PBS, the cells were visualized using a confocal laser scanning microscopy (CLSM, Zeiss LSM-800); (2) the cells were collected, washed twice with PBS, and then analyzed using a flow cytometer (BD, FACSCanto).

2.7 *In vitro* antitumor efficacy

The *in vitro* antitumor efficacy of CPB and SiFeO was evaluated using the Alamar blue assay. MDA-MB-231 and 4T1 cells were seeded in a 96-well plates at a density of 1 × 10^4 cells/well and incubated overnight. Subsequently, the following steps were performed: (1) Various formulations at different concentrations were applied to the cells and incubated for 24 h; (2) various formulations at different concentrations were introduced to the cells for a 6 h incubation, followed by either irradiation or no irradiation with an 808 nm laser (power density: 1 W/cm^2) for 10 min, and then further incubated for another 18 h. After these incubations, the old medium was replaced with a fresh cell culture medium containing 10% Alamar blue, and the cells were incubated for an additional ~ 2 h. The fluorescence (excitation range: 540–570 nm, emission range: 580–610 nm) and absorbance (OD at 570 nm, using 600 nm as a reference wavelength) of the samples were recorded with a microplate reader to evaluate cell viability.

The *in vitro* antitumor effects of CPB and SiFeO were also investigated using live/dead dual-staining assays. In brief, 4T1 cells were plated into 24-well plates at a density of 1.5 × 10^5 cells/well. After overnight incubation, the cells were exposed to different formulations for 5 h (the final concentration of H_2O_2 was 100 μM, and the final concentration of CPB/SiFeO was 100 μg/mL). The cells were either irradiated or left untreated for 10 min with an 808 nm laser (power density: 1 W/cm^2), followed by an additional 24 h incubation. The cells were collected, and a live/dead cell assay was performed. The cells were then observed using a fluorescence microscopy.

For apoptosis assessment, 4T1 cells plated in a 24-well dishes were treated with CPB (50 μg/mL) or SiFeO (50 μg/mL) for 6 h, followed by irradiation or no irradiation for 10 min with an 808 nm laser (power density of 1 W/cm^2). Subsequently, the cells were further incubated for 18 h in a fresh cell culture medium. Afterward, the cells were harvested and stained with Annexin V-FITC and PI for apoptosis assessment. Following a 15 min incubation in the dark, the cells were detected using flow cytometry.

2.8 Intracellular ROS detection

4T1 cells were treated with various samples for 6 h. The samples included the control, H_2O_2 (100 μM), CPB (50 or 100 μg/mL), SiFeO (50 or 100 μg/mL), H_2O_2 (100 μM) + CPB (50 or 100 μg/mL), and H_2O_2 (100 μM) + SiFeO (50 or 100 μg/mL). After the treatment, the medium was removed and the cells were washed several times with PBS. Subsequently, the following steps were performed: (1) Fresh medium containing DCFH-DA was introduced into the cells and incubated for 30 min. The cells were then visualized using a fluorescence microscopy; (2) the treated cells were harvested and incubated with medium containing DCFH-DA for 30 min. The cells were then analyzed using flow cytometry.

2.9 *In vitro* ICD response assessment

ICD was assessed by measuring surface-exposed CRT, ATP release, and HMGB1 secretion. Briefly, 4T1 cells were treated with PBS, CPB (50 μg/mL), or SiFeO (50 μg/mL) for 6 h, followed by laser exposure (808 nm laser, 1 W/cm^2, 10 min). After laser treatment, the old medium was replaced with fresh medium, and the cells were incubated for an additional 18 h. Subsequently, the cells were fixed and stained with anti-CRT (Abcam) at 4 °C overnight, followed by labeled with goat anti-rabbit IgG H&L secondary antibody (Abcam) at room temperature for 1 h. 4',6-Diamidino-2-phenylindole (DAPI) was used to stain the nuclei. Finally, the cells were either visualized using a fluorescence microscopy or analyzed by flow cytometry. Additionally, the supernatants from the cells were collected for ATP detection and HMGB1 ELISA assays.

2.10 Biodistribution and *in vivo* thermal imaging

4T1 cells (5 × 10^5 cells) were transplanted into the subcutaneous fat pad of 6-week-old female BALB/c mice. All animal procedures were carried out following the guidelines for the Care and Use of Laboratory Animals and received authorization from the Laboratory Animal Ethics Committee of Jinan University (IACUC-20210915-02). When the tumors reached approximately 150 mm^3, the mice were intravenously injected with SiFeO. The fluorescence distribution was monitored using the PerkinElmer IVIS Lumina Series III imaging system at 0, 6, 12, 24, 36, and 72 h post-injection. At 24 h post-injection, major organs were excised and subjected to fluorescence imaging using the same imaging system.

For photothermal therapy, 4T1 tumor-bearing mice were treated with SiFeO by intravenous (i.v.) injection. After 24 h, the tumor sites were irradiated with a NIR laser at 1 W/cm^2 for 10 min, and the temperature was monitored using an infrared thermal imaging system.

4T1 tumor-bearing mice, with tumor volumes of ~ 150 mm^3, were intravenously administered SiFeO at a dose of 10 mg/kg. To evaluate the biodistribution and metabolism of SiFeO *in vivo*, samples were collected at specified time points post-injection.

Tumors, major organs, and feces were harvested at 12, 24, 48, and 72 h after injection, while blood samples were obtained at 0.25, 0.5, 2, 4, 8, 12, and 24 h to monitor circulating levels of SiFeO. All samples were analyzed for metal content using inductively coupled plasma mass spectrometry (ICP-OES; ThermoICPOES7200, USA).

2.11 *In vivo* antitumor efficacy evaluation

To assess the *in vivo* antitumor efficacy, 4T1 tumor-bearing mice were randomly assigned to three groups (n = 8): PBS, SiFeO (10 mg/kg), and SiFeO (10 mg/kg) + Laser (SiFeO/Laser). Mice received different treatments according to the treatment schedule. Specifically, mice were treated with SiFeO through intravenous injection twice. Photothermal therapy (irradiation with an 808 nm laser at 1 W/cm^2 for 10 min) was performed 24 h after the second intravenous injection of SiFeO. Tumor volume and body weight were monitored every 2 days. Tumor volume was determined using the formula $V = 0.5 \times A \times B^2$ (where A is the longer diameter and B is the shorter diameter). After 25 days of therapy, the mice were euthanized, and the major organs and tumors were harvested for hematoxylin and eosin (H&E) and immunofluorescence staining. Immunofluorescence staining assays were performed according to the manufacturer's guidelines. Tumor sections were then examined using fluorescence microscopy.

2.12 Statistical analysis

Data were reported as mean ± standard deviation (SD). Statistical analyses were conducted using GraphPad Prism 8. To compare multiple groups, a one-way analysis of variance (ANOVA) was conducted, followed by Tukey's post-hoc analysis. Statistical significance was defined as $P < 0.05$. The levels of significance were denoted as follows: $^*P < 0.05$, $^{**}P < 0.01$, $^{***}P < 0.001$, $^{****}P < 0.0001$; "n.s." denotes not significant. Flow cytometry data were analyzed using FlowJo version 10.8.1, and *in vivo* imaging data were processed with Living Image software version 4.3.1.16427.

3 Results and discussion

3.1 Construction and characterization of SiMOFs and SiFeO

The SiMOFs were synthesized using a microwave-assisted hydrothermal method (Scheme 1(a)). Intriguingly, varying the experimental conditions, such as the ratios of reaction agents, resulted in SiMOFs with distinct structural morphologies, creating a diverse array of SiMOFs. Figures 1(a)–1(h) show both the structural models and transmission electron microscopy (TEM) images of these various SiMOFs. The images included flower-like SiMOFs (SiNFs) in Figs. 1(a) and 1(b), capsule-like SiMOFs (SiNCs) in Figs. 1(c) and 1(d), hexagonal snowflake-like SiMOFs (SiNHSs) in Figs. 1(e) and 1(f), and necklace-like SiMOFs (SiNNs) in Figs. 1(g) and 1(h). The SiNFs and SiNHSs were relatively large, with sizes around 800 nm and 1 μm, respectively. The SiNNs, in contrast, exhibited unique, linearly ordered necklace-like nanostructures composed of periodic hollow nanospheres, each approximately 80 nm in diameter. The TEM image in Fig. 1(d) showed that SiNCs have a uniform capsule shape with an average size of about 200 nm. Most of these nanocapsules appeared collapsed, indicative of their flexible structure. Elemental mapping and energy-dispersive X-ray spectroscopy (EDS) spectra (Figs. S1–S3 in the Electronic Supplementary Material (ESM)) confirmed the presence of elements like C, N, O, Zn, and Si in the SiMOFs, regardless of their morphological variations. The creation of SiMOFs with these diverse morphologies demonstrated the versatility and effectiveness of this synthetic approach.

Given their high porosity and ample interior space, SiMOFs were deemed excellent candidates for drug loading and delivery. The process of preparing drug-loaded SiNCs is illustrated in Fig. 1(i). Initially, curcumin was introduced to SiNCs, forming SiNCs@Curcumin after a 24 h incubation period. These SiNCs@Curcumin were then reacted with Prussian blue to create iron-based nanoparticles on the SiNCs and then modified with PVP, resulting in the formation of the nanocomposites SiFeO with good water dispersibility, which comprised SiNCs loaded with both curcumin (curcumin loading content: 11%) and iron-based nanoparticles. The UV–Vis spectrum of SiNCs@Curcumin, shown in Fig. 1(j) (pink line), displayed a distinct absorption peak at around 405 nm, confirming the presence of curcumin. In contrast, iron-based nanoparticles (referred to as CPB), produced using curcumin and Prussian blue as precursors, showed a weaker absorption peak at ~ 405 nm and a prominent one at ~ 700 nm (green line). SiFeO exhibited absorption peaks at both these wavelengths (red line), indicating the formation of iron-based nanoparticles on SiNCs through the interaction of curcumin and Prussian blue. Images corresponding to these samples were presented in the right panel of Fig. 1(j). TEM images (Fig. 1(k)) revealed that SiNCs@Curcumin had a larger size (~ 280 nm) compared to SiNCs, possibly due to reduced nanostructure collapse from curcumin loading. Figure 1(l) shows the morphology of SiFeO, similar in size to SiNCs@Curcumin. Additionally, the TEM image of SiFeO displayed nanoparticles on the nanocapsules, verifying the presence of iron-based nanoparticles on SiNCs. CPB, in contrast, exhibited aggregated morphology with larger size and poor dispersibility (Fig. S4 in the ESM). EDS spectra and elemental mappings (Fig. S5 in the ESM) confirmed the presence of C, N, O, and Fe elements in CPB. SiFeO, as depicted in Fig. 1(m), displayed Si, Zn, N, C, O, and Fe signals, affirming the incorporation of iron-based nanoparticles on SiNCs. Elemental mappings (Fig. 1(n)) showed a uniform distribution of Si, Zn, C, N, and O, while Fe was localized, consistent with the TEM results. SiNCs nanocapsules were around 200 nm in size, smaller than SiNCs@Curcumin (~ 280 nm) and SiFeO (~ 280 nm) observed via TEM (Figs. 1(d), 1(k), and 1(l)). However, SiNCs, SiNCs@Curcumin, and SiFeO shared a similar hydrodynamic diameter of ~ 350 nm (Fig. 1(o)), attributed to the flexible structures of the nanocapsules, which could spread out in aqueous solutions. SiFeO exhibited a significantly negative zeta potential (–22.6 mV) compared to SiNCs (–5.04 mV) due to the abundance of negatively charged curcumin (Fig. 1(p)). By tracking the hydrodynamic diameter over time, we observed that SiFeO remained stable in water for up to 96 h, with no significant variation in particle size (Fig. S6 in the ESM). Additionally, we analyzed the nitrogen adsorption–desorption isotherms and Barrett–Joyner–Halenda (BJH) pore size distributions for SiNCs and SiFeO. These measurements highlighted the porous nature of SiNCs. Specifically, the Brunauer–Emmett–Teller (BET) surface area of SiNCs was found to be 30.5 m^2/g, indicating a high surface area conducive to drug loading. SiNCs exhibited a mesoporous structure with a pore size of approximately 29.4 nm, ideal for accommodating drug molecules (Fig. S7(a) in the ESM). After drug loading to form SiFeO, both the

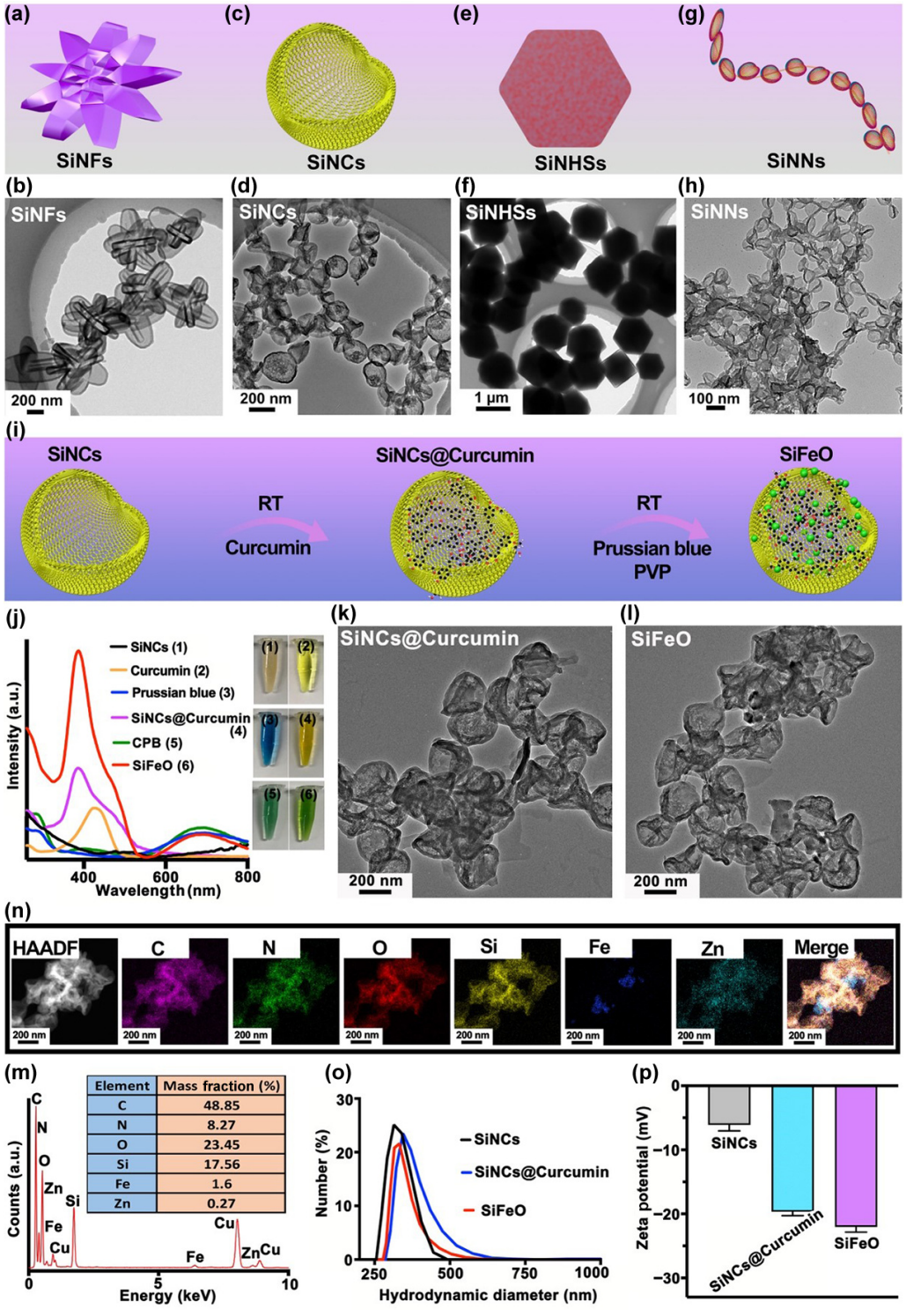

Figure 1 Characterizations of SiMOFs and SiFeO. (a)–(h) Structure models and TEM images of SiMOFs with various structures. (i) Preparation diagram of SiFeO. (j) UV–Vis absorption spectra of various samples. TEM images of (k) SiNCs@curcumin and (l) SiFeO. (m) The EDS spectra of SiFeO. (n) Elemental distribution mapping images of SiFeO. (o) hydrodynamic diameter and (p) zeta potential of different formulations.

BET surface area and pore diameter decreased significantly, with the BET surface area reducing to 18.4 m^2/g and the pore size decreasing to around 11.2 nm (Fig. S7(b) in the ESM). This marked reduction in surface area and pore size suggested that the pores of SiNCs were effectively occupied by the drugs, confirming successful drug loading.

3.2 ROS generation measurements in SiFeO for chemodynamic therapy

CDT relies on the generation of highly reactive hydroxyl radicals (·OH) to kill tumor cells [21]. To assess whether SiFeO nanoparticles could produce ·OH, we used TMB as a detector. As depicted in Fig. 2(a), incubating TMB with a control compound

(CPB) and hydrogen peroxide (H_2O_2) at pH 7.0 resulted in the emergence of a clear peak at 652 nm in the UV–Vis spectrum, revealing the generation of ·OH and the formation of oxidized TMB (ox-TMB). The absorbance peak of oxidized TMB at 652 nm exhibited a substantial increase when TMB was incubated with both CPB and H_2O_2 at pH 5.5, as illustrated in Fig. 2(b). This observation indicated the heightened capability of CPB for ·OH generation under acidic conditions.

Similarly, we investigated SiFeO's ability to catalyze H_2O_2 decomposition. Under neutral pH (7.0), the group containing TMB, SiFeO, and H_2O_2 (green line) showed no noticeable peak at 652 nm (Fig. 2(c)), suggesting limited ·OH generation. However, the same group at a lower pH (5.5) displayed a robust peak at 652 nm (Fig. 2(d)), indicating strong ·OH production by SiFeO under mildly acidic conditions. These results indicated that SiFeO, particularly due to its iron-based nanoparticles, was highly effective in generating ROS, especially under mildly acidic conditions (pH 5.5). This efficacy positioned SiFeO as a potential nanodrug candidate for chemodynamic cancer therapy, exploiting its ability to catalyze the production of toxic ·OH radicals in tumor environments.

3.3 Photothermal effect of SiFeO

Motivated by their NIR absorption (Fig. 1(j)), we investigated the photothermal properties of CPB and SiFeO. Both materials (Fig. 2(e)–2(h)) displayed concentration- and power-density-dependent temperature increases, confirming their strong photothermal efficiency. At 808 nm laser (1.0 W/cm², 20 min), pure water's ΔT remained low (< 6.0 °C), while CPB's ΔT rose from 6.5 to 39.1 °C as concentration increased from 5 to 200 μg/mL. SiFeO mirrored this trend (Fig. 2(f)), reaching a ΔT of 32.4 °C at 200 μg/mL. Notably, both CPB and SiFeO exhibited excellent photothermal stability. Over four heating/cooling cycles (Fig. 2(i)), their maximum temperatures remained nearly constant, showcasing their potential for repeated photothermal applications. These findings collectively indicated that SiFeO, with its iron-based nanoparticles incorporated within the SiMOFs structure, possessed outstanding photothermal properties, highlighting its potential for photothermal therapy.

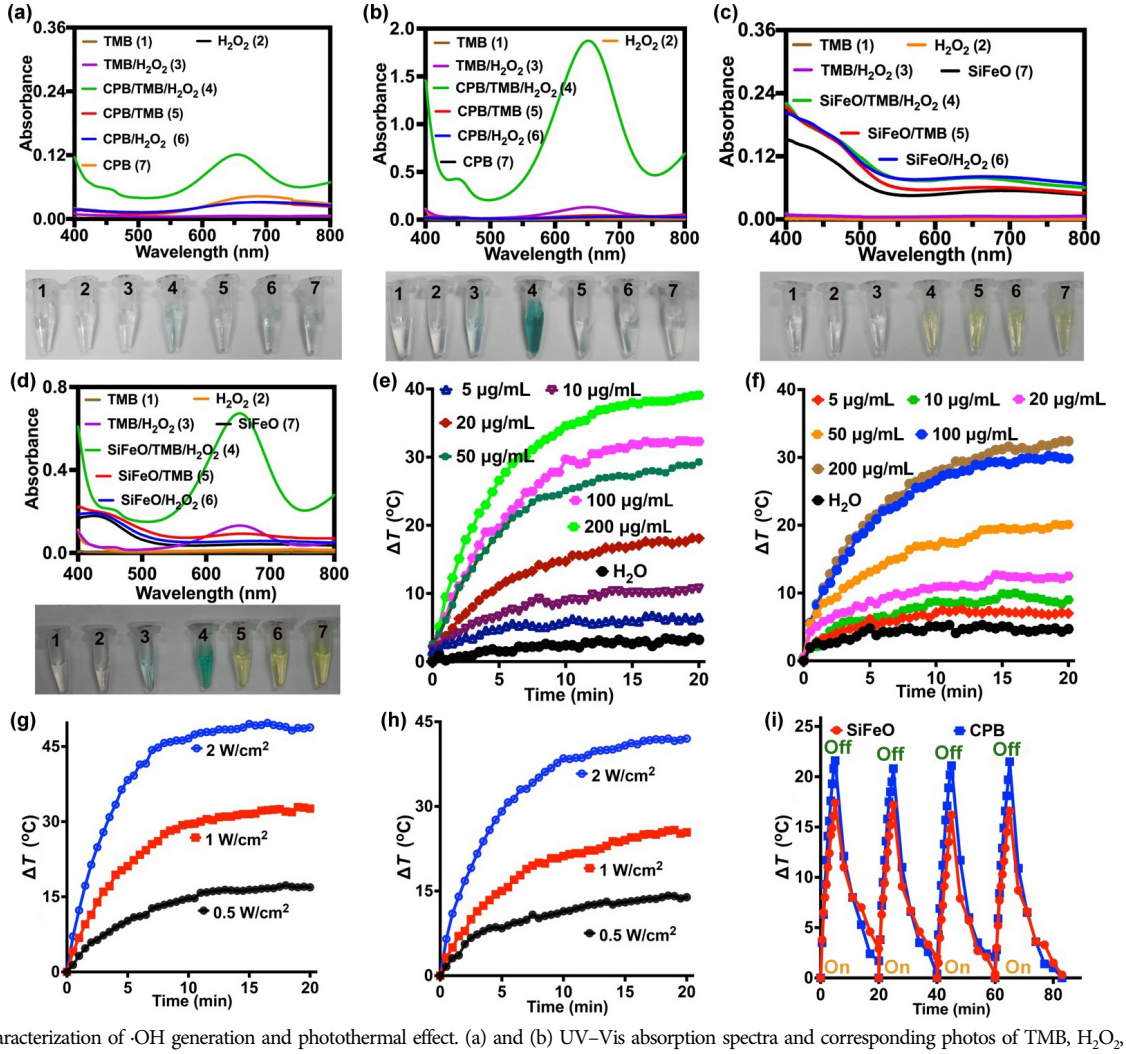

Figure 2 Characterization of ·OH generation and photothermal effect. (a) and (b) UV–Vis absorption spectra and corresponding photos of TMB, H_2O_2, TMB/H_2O_2, CPB/TMB/H_2O_2, CPB/TMB, CPB/H_2O_2 and CPB at pH 7.0 and 5.5. (c) and (d) UV–Vis absorption spectra and corresponding photos of TMB, H_2O_2, TMB/H_2O_2, SiFeO/TMB/H_2O_2, SiFeO/TMB, SiFeO/H_2O_2, and SiFeO at pH 7.0 and 5.5. In (a)–(d), [CPB] = 20 μg/mL, [SiFeO] = 20 μg/mL, [TMB] = 0.2 mM, [H_2O_2] = 2 mM. Photothermal curves of CPB (e) and SiFeO (f) with various concentrations under an 808 nm laser irradiation at 1 W/cm², respectively. ΔT curves of (g) CPB solution (100 μg/mL) and (h) SiFeO solution (100 μg/mL) irradiated with 808 nm laser with different power densities for 20 min. (i) ΔT curves of CPB and SiFeO in aqueous phase under four times on/off cycles.

3.4 *In vitro* therapeutic ability

Encouraged by SiFeO's excellent photothermal conversion capacity and impressive ROS generation ability, we evaluated its *in vitro* therapeutic efficacy. First, we assessed the cellular uptake of SiFeO using confocal laser scanning microscopy and flow cytometry. The results indicated that Cy7-labeled SiFeO was efficiently internalized by 4T1 cells, demonstrating high uptake efficiency (Fig. S8 in the ESM). Alamar blue assay revealed SiFeO's dose-dependent cytotoxicity against tumor cells, unlike CPB, which displayed minimal toxicity (Figs. 3(a) and 3(b)). This potency of SiFeO may be attributed to the encapsulated curcumin (Fig. S9 in the ESM) and the generation of toxic ROS. Further evaluation of CPB and SiFeO cytotoxicity on MDA-MB-231 cells (Fig. S10 in the ESM) indicated that CPB had minimal effect, even at high concentrations (50 μg/mL). In contrast, SiFeO demonstrated significant, dose-dependent cytotoxicity in these cells. Under laser irradiation, SiFeO's effectiveness was markedly enhanced, with the SiFeO/Laser group destroying about 80% of 4T1 cells at 50 μg/mL, underlining the efficacy of combined CT-CDT-PTT treatments. Live/dead staining further supported these findings, showing that both CPB/Laser and SiFeO/Laser treatments possessed potent tumor cell-killing capacities, independent of the presence of H_2O_2 (Fig. 3(c)). Oxidative stress analysis using the DCFH-DA probe showed negligible stress in control groups but significant fluorescence in SiFeO-treated 4T1 cells, indicating increased oxidative stress (Fig. 3(d)). This was particularly intense in the SiFeO/H_2O_2 group, as supported by flow cytometry data (Fig. S11 in the ESM). Cell death analysis using Annexin V-FITC/PI double staining showed that CPB under NIR laser irradiation (CPB/Laser) induced an apoptosis rate of 33%, which was significantly higher than the 19.2% rate triggered by CPB alone (Figs. 3(e) and 3(f)). However, SiFeO led to a strikingly high apoptosis rate of 76.1%, likely due to combined chemotherapy/oxidation damage. The SiFeO/Laser group showed the highest tumor apoptosis rate at 89.9%, with 69.5% early apoptotic and 20.4% late apoptotic cells. These results suggested SiFeO's potential as an effective agent for tumor therapy, capable of inducing strong oxidative stress and high apoptosis rates, especially when combined with laser irradiation.

3.5 *In vitro* ICD induction ability

Inducing ICD is a promising strategy in cancer therapy, as it can transform immunosuppressive "cold" tumors into immunologically

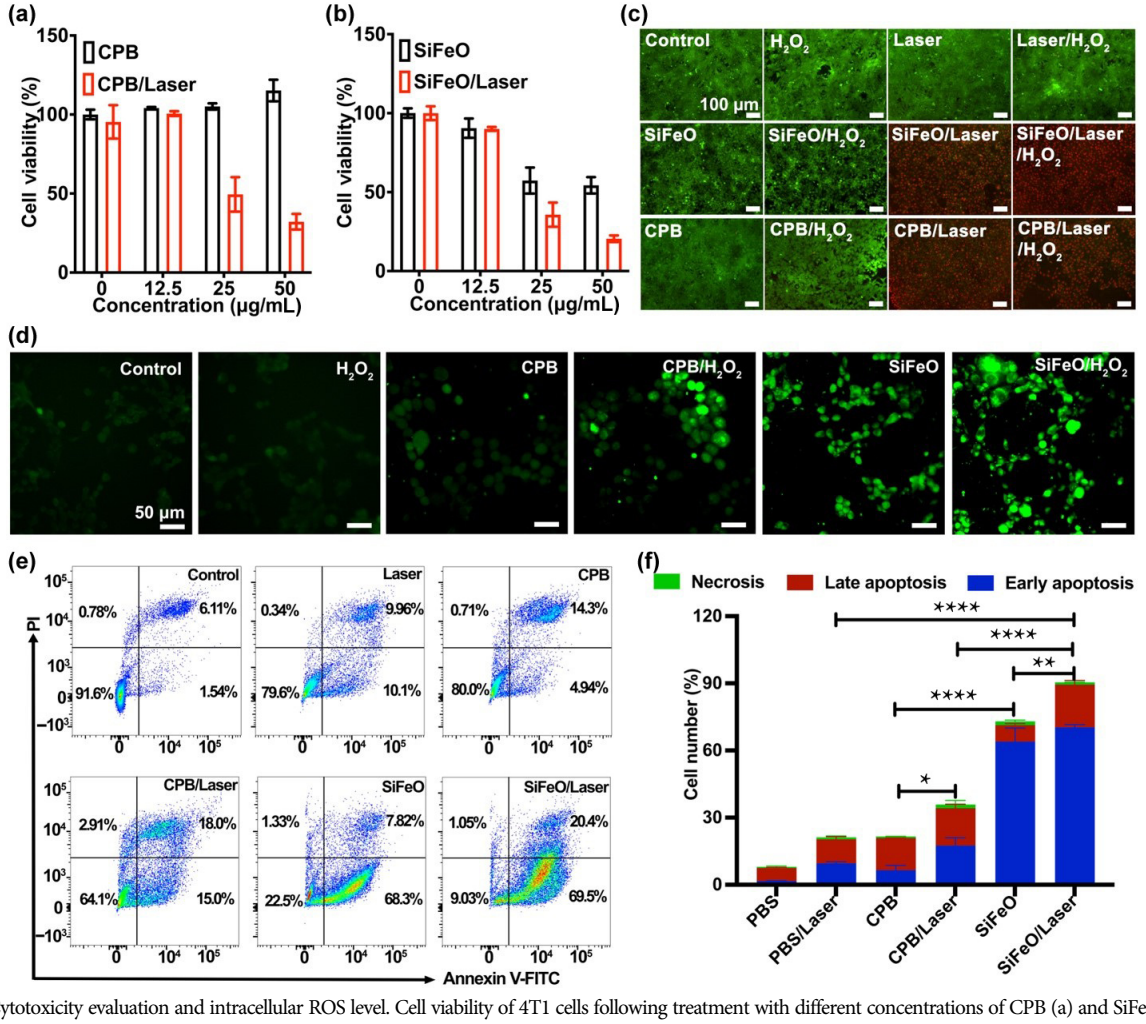

Figure 3 Cytotoxicity evaluation and intracellular ROS level. Cell viability of 4T1 cells following treatment with different concentrations of CPB (a) and SiFeO (b) under conditions with and without laser irradiation. (c) Live/dead staining of 4T1 cells treated with different formulations. (d) Intracellular ROS level observed by a fluorescence microscope after various treatments. (e) Flow cytometric analysis to assess apoptosis in 4T1 cells following different treatments by staining with Annexin V-FITC/PI. (f) Quantitative comparison of apoptosis assay. $n = 3$ for all experiments. To evaluate statistical significance, we employed a one-way ANOVA and conducted Tuey's post-hoc test to compare group means. *P* values: $^{*}p < 0.05$, $^{**}p < 0.01$, $^{****}p < 0.0001$.

active "hot" tumors [22–28]. The key players in ICD are DAMPs such as CRT, HMGB1, and ATP, which stimulate immune responses by promoting the maturation of dendritic cells and the infiltration of cytotoxic T lymphocytes, thereby enhancing antitumor immunity [29, 36, 53, 54]. Encouraged by the excellent therapeutic effect of SiFeO on 4T1 cells via synergistic CT-CDT-PTT therapy, we evaluated its ability to induce ICD by assessing the exposure and release of DAMPs at the cellular level (Fig. 4). Immunofluorescence staining was employed to detect the translocation of CRT to the plasma membrane, a hallmark of ICD. Minimal CRT translocation was observed in the PBS, Laser alone, and CPB groups, indicating that these treatments did not significantly induce ICD. In contrast, significant CRT exposure was detected in the SiFeO group and the CPB/Laser group, suggesting that SiFeO can induce ICD through chemotherapy and chemodynamic therapy, while CPB combined with laser irradiation can induce ICD primarily via photothermal treatment. Notably, the SiFeO/Laser group exhibited the strongest CRT translocation, indicating an enhanced ability to induce CRT exposure under laser irradiation (Figs. 4(a) and 4(b)). These findings suggested that SiFeO, when combined with laser irradiation, effectively promoted CRT translocation through the synergistic effects of CT-CDT-PTT therapy. Flow cytometry analysis further confirmed increased CRT exposure in the SiFeO and SiFeO/Laser groups (Fig. 4(c)). We also measured extracellular levels of HMGB1 using an ELISA assay. Elevated HMGB1 levels were observed in the CPB/Laser and SiFeO/Laser groups, indicating that HMGB1 was released from the nucleus into the extracellular matrix due to plasma membrane disruption (Fig. 4(d)). Additionally, ATP secretion was significantly increased in the CPB/Laser group, reflecting the effectiveness of photothermal therapy. Notably, the SiFeO group demonstrated substantial ATP release even without laser irradiation, attributable to SiFeO's potent tumor cell-killing capacity via combined chemotherapy and chemodynamic therapy. The highest ATP secretion was observed in the SiFeO/Laser group (Fig. 4(e)). These results indicated that SiFeO-mediated CT-CDT-PTT combination therapy effectively triggered ICD by releasing multiple DAMPs through synergistic mechanisms, potentially reversing the immunosuppressive tumor microenvironment and enhancing the antitumor immune response.

3.6 *In vivo* antitumor study

We investigated the antitumor effects of SiFeO-mediated combination therapy *in vivo* using a 4T1 tumor-bearing BALB/c mouse model. Initially, we tracked the *in vivo* distribution of SiFeO labeled with NIR-emitting Cy7 dye (Fig. S12(a) in the ESM). Post-injection imaging revealed maximum fluorescence at the tumor site 24 h after injection, persisting beyond 72 h (Figs. S12(b) and S12(c) in the ESM). The effective accumulation of SiFeO at the tumor site was likely attributed to the enhanced permeability and retention (EPR) effect [55]. This accumulation was also confirmed through *ex vivo* imaging of tumor tissues and major organs (Fig. S12(d) in the ESM). After 24 h of SiFeO injection, tumor sites in mice were subjected to an 808 nm laser for 10 min at a power density of 1 W/cm^2. Thermal imaging revealed a substantial temperature increase, reaching 52 °C. These findings suggested that SiFeO could effectively accumulate in tumors for CT-CDT-PTT combination therapy (Figs. S12(e) and S12(f) in the ESM). Additionally, we

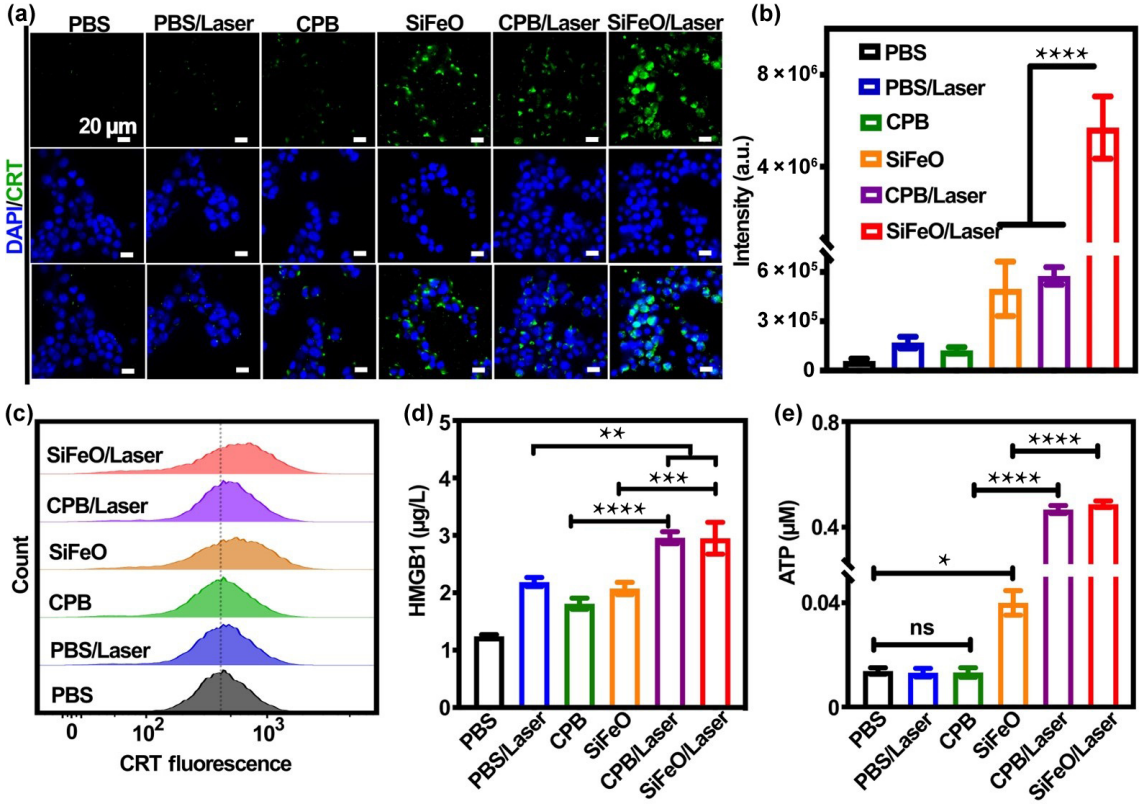

Figure 4 *In vitro* ICD. (a) Fluorescent images to show CRT translocation on cell membranes in terms of different treatments. (b) CRT quantification analysis corresponding to panel (a). (c) Flow cytometric assessment of CRT exposure on the surface of 4T1 cells after different treatments. Quantitative analysis of the HMGB1 release (d) and ATP secretion (e) in 4T1 tumor cells upon diversified regimens. $n = 3$ for all experiments. To evaluate statistical significance, we employed a one-way ANOVA and conducted Tukey's post-hoc test to compare group means. p values: $^*p < 0.05$, $^{**}p < 0.01$, $^{***}p < 0.001$, $^{****}p < 0.0001$, n.s. stands for not significant.

analyzed the pharmacokinetic profile of SiFeO to assess its metabolic behavior. Following i.v. injection of SiFeO, its biodistribution in major organs, tumors, and fecal samples was assessed at various time points using ICP-OES (Fig. S13 in the ESM). The results showed efficient accumulation of SiFeO in tumor sites, consistent with our *in vivo* imaging data. Similar to many other nanomaterials, SiFeO preferentially accumulated in the liver, likely due to uptake by the cells of the reticuloendothelial system. Analysis of fecal samples demonstrated effective excretion of Fe, Si, and Zn over time, indicating that SiFeO can be metabolized and cleared from the body. Additionally, we assessed the pharmacokinetics of SiFeO by measuring the concentration of Fe in the bloodstream at various time points after intravenous injection using ICP-OES (Fig. S14 in the ESM). A two-compartment exponential model was developed to simulate the elimination kinetics of Fe levels in the bloodstream, with the distribution and elimination phase half-lives determined to be 0.44 and 13.6 h, respectively.

The antitumor efficacy of SiFeO was further evaluated in three groups of mice (n = 8): treated with PBS, SiFeO, and SiFeO plus laser irradiation (SiFeO/Laser) when the tumors reached approximately 150 mm^3 (Fig. 5(a)). Throughout the treatment period, mice in the SiFeO and SiFeO/Laser groups exhibited stable body weights without significant fluctuations, comparable to those in the PBS control group, as shown in Fig. 5(b). These results suggested that both SiFeO and SiFeO/Laser treatments caused minimal systemic toxicity. We assessed the hemocompatibility of SiFeO by measuring the hemolysis rate of blood samples treated with various concentrations of SiFeO. The hemolysis rate remained below 5% even at a high concentration of 1000 μg/mL, indicating

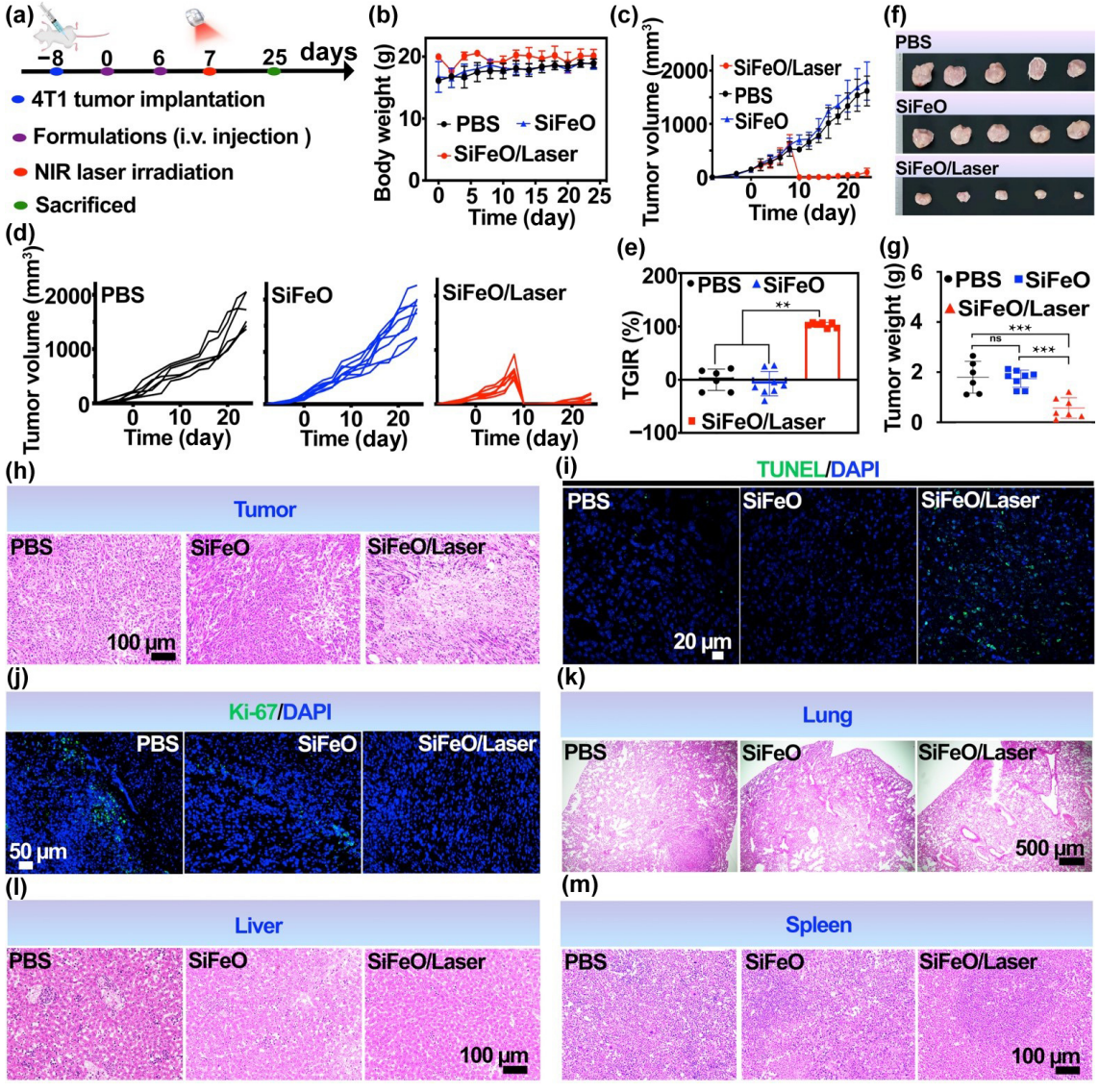

Figure 5 Antitumor efficacy of SiFeO *in vivo*. (a) Schematic description of antitumor activity of SiFeO using 4T1 tumor-bearing BALB/c female mice model. (b) Body weight changes during the treatment period. (c) Tumor volume growth profiles of mice. (d) Individual tumor growth curves depicting the progression of 4T1 tumors in mice subjected to various treatments. (e) TGIR in different treatment groups. (f) Photographs depicting representative tumors from various treatment groups on the 25th day. (g) The weight of separated tumors after different treatments. Representative images of H&E staining (h), TUNEL staining (i), and Ki-67 staining (j) of tumor slices harvested from mice treated with various formulations. Representative H&E-stained images of the lung (k), liver (l), and spleen tissues (m). n = 5–8. To evaluate statistical significance, we employed a one-way ANOVA and conducted Tukey's post-hoc test to compare group means. p values: $^{**}p < 0.01$, $^{***}p < 0.001$, n.s. stands for not significant.

good hemocompatibility (Fig. S15 in the ESM). Furthermore, the *in vivo* toxicity of SiFeO was evaluated by analyzing blood biochemical parameters. No significant abnormalities were detected compared to the control group (Fig. S16 in the ESM). H&E staining of major organs showed no apparent tissue damage or pathological changes (Fig. S17 in the ESM). These findings collectively demonstrated that SiFeO possessed excellent biocompatibility and low toxicity, highlighting its potential for safe use in biomedical applications. Tumor growth analysis revealed that SiFeO alone had a minimal effect on tumor suppression. In contrast, SiFeO combined with laser treatment significantly inhibited tumor growth, as illustrated in Figs. 5(c)–5(g). Specifically, this significant inhibition was evidenced by a higher tumor growth inhibition rate (TGIR) (Fig. 5(e)) and smaller tumor mass in the SiFeO/Laser group (Fig. 5(g)). H&E and TUNEL staining further indicated increased nuclear injury and apoptosis in this group, compared to the PBS and SiFeO groups (Figs. 5(h) and 5(i)). Ki-67 staining showed reduced cell proliferation in the SiFeO/Laser group, confirming the extensive apoptosis triggered by this treatment (Fig. 5(j)). Metastasis was assessed through H&E staining of lung and liver tissues. Results showed that SiFeO/Laser treatment inhibited tumor metastasis (Figs. 5(k) and 5(l)). Splenomegaly, a common symptom in 4T1 tumor-bearing mice [46, 56, 57], was also evaluated. H&E-stained spleen slices from the SiFeO/Laser group showed normal splenic architecture, contrasting with swollen spleens in the PBS and SiFeO groups (Fig. 5(m) and Fig. S18(a) in the ESM). Spleen weights were significantly reduced in the SiFeO/Laser group, indicating effective mitigation of splenomegaly (Fig. S18(b) in the ESM). In summary, these findings collectively demonstrated the potent therapeutic efficacy of SiFeO in combination with laser irradiation, highlighting its potential for effective cancer treatment.

3.7 Antitumor immune response induced by SiFeO/Laser treatment

To explore the mechanism responsible for the potent antitumor activity observed in the SiFeO/Laser group, we conducted immunofluorescence staining of tumor tissue slices after various treatments, as shown in Fig. 6. The strongest CRT signals, a vital ICD biomarker, were observed in the SiFeO/Laser group (Figs. 6(b) and 6(c)). This indicated a significant translocation of CRT to the plasma membrane, suggesting potent ICD induction by SiFeO/Laser treatment. The phenotypes of tumor-associated macrophages (TAMs), which can either suppress (M2) or promote (M1) tumor immunity [53, 58–61] were also assessed. The SiFeO/Laser treatment group showed reduced CD206 signals, a hallmark of M2 macrophages, indicating a decrease in immunosuppressive M2 macrophages in the tumor microenvironment (Figs. 6(d) and 6(e)). Antigen-presenting cells (APCs) are crucial in the immune system's response to tumors, prominently enhancing antitumor immunity. CD80 and CD86 are

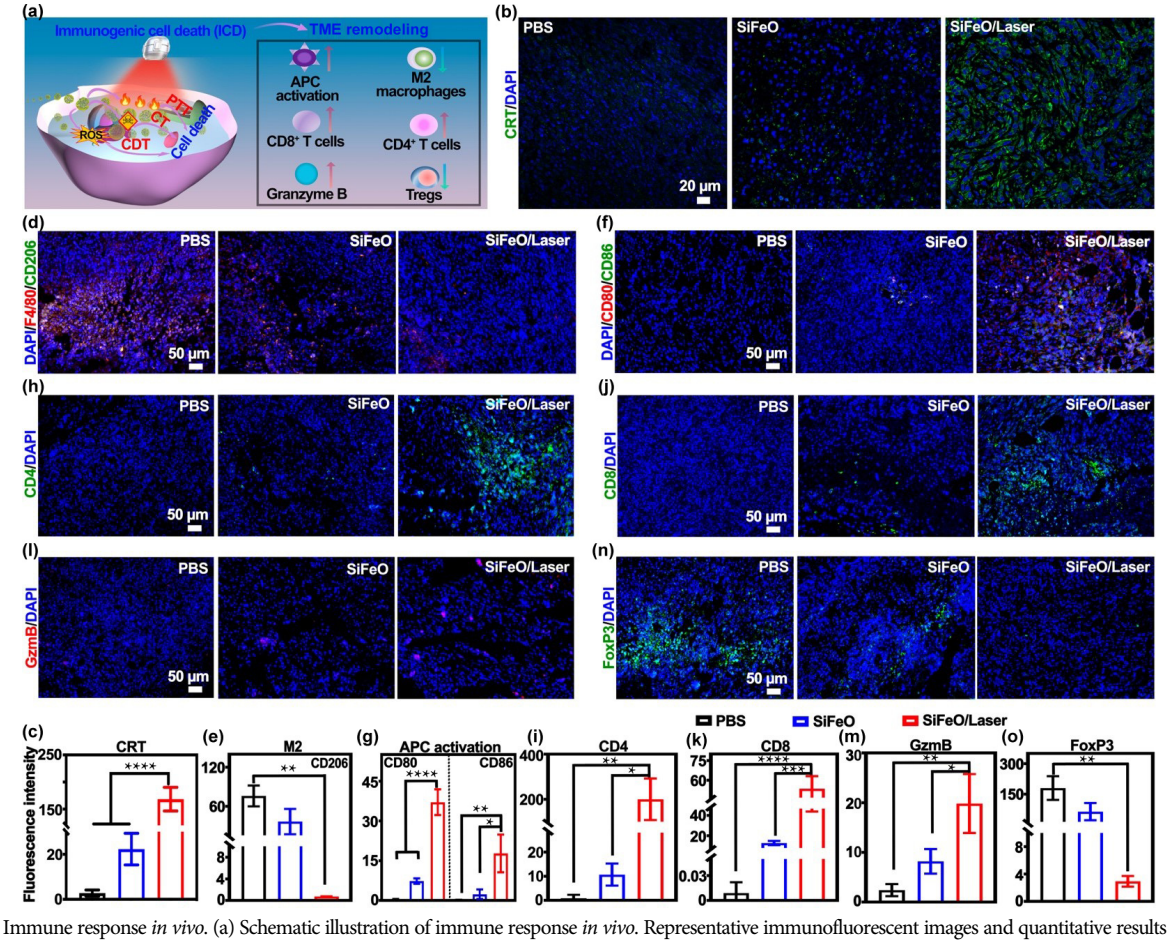

Figure 6 Immune response *in vivo*. (a) Schematic illustration of immune response *in vivo*. Representative immunofluorescent images and quantitative results of CRT (b) and (c), CD206 (a hallmark of M2 macrophages) (d) and (e), CD80 and CD86 (hallmarks of APC activation) (f) and (g), CD4 (h) and (i), CD8 (j) and (k), GzmB (l) and (m), FoxP3 (n) and (o) expression in tumors. To evaluate statistical significance, we employed a one-way ANOVA and conducted Tukey's post-hoc test to compare group means. *p* values: $^{*}p < 0.05$, $^{**}p < 0.01$, $^{***}p < 0.001$, $^{****}p < 0.0001$.

key markers indicating APC activation and their preparedness to stimulate T cells and enhance antitumor responses [62–64]. In our study, the SiFeO/Laser treatment group exhibited significantly higher expression levels of CD80 and CD86 in tumor tissues, as shown in Figs. 6(f) and 6(g). This suggested that SiFeO/Laser therapy effectively promoted APC activation, thereby enhancing antitumor immune responses. An increase in both $CD4^+$ and $CD8^+$ T cells was noted in the SiFeO/Laser treatment group (Figs. 6(h)–6(k)), indicating enhanced infiltration of these cells into the tumor tissues. This shift was critical for transforming the TME from "cold" to "hot". Granzyme B (GzmB), a cytotoxic protein secreted by $CD8^+$ T cells, was found at the highest levels in the SiFeO/Laser group. This indicated the significant immunostimulatory effect of the treatment (Figs. 6(l) and 6(m)). Finally, the SiFeO/Laser group exhibited a decrease in Foxp3 signals (Figs. 6(n) and 6(o)), a marker for regulatory T cells (Tregs) known for their immunosuppressive functions [65]. The reduction of Tregs in this group suggested a less immunosuppressive TME. These findings collectively confirmed that SiFeO/Laser treatment exhibited excellent antitumor activity due to the activation of robust antitumor immune responses via the induction of ICD.

4 Conclusions

Using rapid microwave synthesis, we synthesized diverse SiMOFs with unique flower-like, capsule-like, hexagonal snowflake-like, and necklace-like morphologies. Notably, these high-porosity SiMOFs excelled as drug carriers. We loaded capsule-like SiMOFs (SiNCs) with curcumin (SiNCs@Curcumin) and then modified them with Prussian blue to incorporate iron-based nanoparticles, generating SiFeO. SiFeO, with its excellent photothermal effects and high capacity for generating ROS, can effectively kill tumor cells through chemotherapy, chemodynamic therapy, and photothermal therapy. This multi-pronged CT-CDT-PTT approach effectively triggered ICD, marked by the exposure or the release of multiple DAMPs, including surface-exposed CRT, released ATP, and secreted HMGB1. SiFeO with NIR laser displayed remarkable antitumor efficacy. Immunofluorescence analysis revealed significant modulation of the tumor microenvironment, characterized by a decrease in M2 macrophages, increased activation of APCs, enhanced infiltration of $CD4^+$ and $CD8^+$ T cells, elevated levels of Granzyme B, and a reduction in regulatory T cells. Notably, SiFeO showed promise in synergistic treatment strategies for inducing ICD and boosting antitumor immunity. This work enriches the SiMOF library and highlights their potential in cancer immunotherapy, motivating further exploration of SiMOFs in other biomedical applications.

Electronic Supplementary Material: Supplementary material (materials and chemicals, characterization, and some additional experimental results (e.g., EDS, TEM, stability, nitrogen adsorption–desorption isotherms, Barrett–Joyner–Halenda (BJH) pore size distributions, cellular uptake, cytotoxicity, ROS generation, biodistribution, photothermal imaging, pharmacokinetic profile, hemolysis results, H&E staining, blood biochemistry, spleen photos, and spleen weight)) is available in the online version of this article at https://doi.org/10.26599/NR.2025.94907080.

Data availability

All data needed to support the conclusions in the paper are presented in the manuscript and the Electronic Supplementary Material. Additional data related to this paper may be requested from the corresponding author upon request.

Acknowledgements

We acknowledge support from the Basic and Applied Basic Research Foundation of Guangdong Province, China (No. 2021A1515220001).

Declaration of competing interest

All the contributing authors report no conflict of interests in this work.

Author contribution statement

M. H.: Data curation, validation, experimental design. Z. S. C.: Data curation, validation, experimental design. S. Y. Z.: Data curation, validation, experimental design. Z. D. L.: Data curation, validation. X. T. Y.: Data curation, validation. Y. H.: Project administration, writing manuscript. Y. L. Z.: Project administration, funding acquisition, writing manuscript. K. W. L.: Project administration, funding acquisition, writing manuscript. All the authors have approved the final manuscript.

Informed consent

Not applicable.

Ethics statement

All animal procedures were carried out following the guidelines for the Care and Use of Laboratory Animals and received authorization from the Laboratory Animal Ethics Committee of Jinan University (IACUC-20210915-02).

Use of AI statement

None.

References

[1] Croissant, J. G.; Butler, K. S.; Zink, J. I.; Brinker, C. J. Synthetic amorphous silica nanoparticles: Toxicity, biomedical and environmental implications. *Nat. Rev. Mater.* **2020**, *5*, 886–909.

[2] Park, J. H.; Gu, L.; von Maltzahn, G.; Ruoslahti, E.; Bhatia, S. N.; Sailor, M. J. Biodegradable luminescent porous silicon nanoparticles for *in vivo* applications. *Nat. Mater.* **2009**, *8*, 331–336.

[3] Manzano, M.; Vallet-Regí, M. Mesoporous silica nanoparticles for drug delivery. *Adv. Funct. Mater.* **2020**, *30*, 1902634.

[4] Zhong, Y. L.; Sun, X. T.; Wang, S. Y.; Peng, F.; Bao, F.; Su, Y. Y.; Li, Y. Y.; Lee, S. T.; He, Y. Facile, large-quantity synthesis of stable, tunable-color silicon nanoparticles and their application for long-term cellular imaging. *ACS Nano* **2015**, *9*, 5958–5967.

[5] Zhong, Y. L.; Peng, F.; Bao, F.; Wang, S. Y.; Ji, X. Y.; Yang, L.; Su, Y. Y.; Lee, S. T.; He, Y. Large-scale aqueous synthesis of fluorescent and biocompatible silicon nanoparticles and their use as highly photostable biological probes. *J. Am. Chem. Soc.* **2013**, *135*, 8350–8356.

[6] Zhong, Y. L.; Song, B.; Shen, X. B.; Guo, D. X.; He, Y. Fluorescein sodium ligand-modified silicon nanoparticles produce ultrahigh fluorescence with robust PH- and photo-stability. *Chem. Commun.* **2018**, *55*, 365–368.

[7] Zhong, Y. L.; Chu, B. B.; Bo, X.; He, Y.; Zhao, C. Aqueous synthesis of three-dimensional fluorescent silicon-based nanoscale networks featuring unusual anti-photobleaching properties. *Chem. Commun.* **2019**, *55*, 652–655.
[8] Baraban, L.; Ibarlucea, B.; Baek, E.; Cuniberti, G. Hybrid silicon nanowire devices and their functional diversity. *Adv. Sci.* **2019**, *6*, 1900522.
[9] Vallet-Regí, M.; Schüth, F.; Lozano, D.; Colilla, M.; Manzano, M. Engineering mesoporous silica nanoparticles for drug delivery: Where are we after two decades. *Chem. Soc. Rev.* **2022**, *51*, 5365–5451.
[10] Knežević, N. Ž.; Kaluđerović, G. N. Silicon-based nanotheranostics. *Nanoscale* **2017**, *9*, 12821–12829.
[11] Liu, S. N.; Dou, K. K.; Liu, B.; Pang, M. L.; Ma, P. A.; Lin, J. Construction of multiform hollow-structured covalent organic frameworks via a facile and universal strategy for enhanced sonodynamic cancer therapy. *Angew. Chem., Int. Ed.* **2023**, *62*, e202301831.
[12] Peng, F.; Su, Y. Y.; Zhong, Y. L.; Fan, C. H.; Lee, S. T.; He, Y. Silicon nanomaterials platform for bioimaging, biosensing, and cancer therapy. *Acc. Chem. Res.* **2014**, *47*, 612–623.
[13] Dasog, M.; Kehrle, J.; Rieger, B.; Veinot, J. G. C. Silicon nanocrystals and silicon-polymer hybrids: Synthesis, surface engineering, and applications. *Angew. Chem., Int. Ed.* **2016**, *55*, 2322–2339.
[14] Gao, A. R.; Zou, N. L.; Dai, P. F.; Lu, N.; Li, T.; Wang, Y. L.; Zhao, J. L.; Mao, H. J. Signal-to-noise ratio enhancement of silicon nanowires biosensor with rolling circle amplification. *Nano Lett.* **2013**, *13*, 4123–4130.
[15] He, Y.; Su, S.; Xu, T. T.; Zhong, Y. L.; Zapien, J. A.; Li, J.; Fan, C. H.; Lee, S. T. Silicon nanowires-based highly-efficient SERS-active platform for ultrasensitive DNA detection. *Nano Today* **2011**, *6*, 122–130.
[16] Cheng, Y. J.; Hu, J. J.; Qin, S. Y.; Zhang, A. Q.; Zhang, X. Z. Recent advances in functional mesoporous silica-based nanoplatforms for combinational photo-chemotherapy of cancer. *Biomaterials* **2020**, *232*, 119738.
[17] Jeong, M.; Jung, Y.; Yoon, J.; Kang, J. Y.; Lee, S. H.; Back, W.; Kim, H.; Sailor, M. J.; Kim, D.; Park, J. H. Porous silicon-based nanomedicine for simultaneous management of joint inflammation and bone erosion in rheumatoid arthritis. *ACS Nano* **2022**, *16*, 16118–16132.
[18] Kim, B.; Sun, S.; Varner, J. A.; Howell, S. B.; Ruoslahti, E.; Sailor, M. J. Securing the payload, finding the cell, and avoiding the endosome: Peptide-targeted, fusogenic porous silicon nanoparticles for delivery of SiRNA. *Adv. Mater.* **2019**, *31*, 1902952.
[19] Gong, W.; Chen, Z. J.; Dong, J. Q.; Liu, Y.; Cui, Y. Chiral metal-organic frameworks. *Chem. Rev.* **2022**, *122*, 9078–9144.
[20] Freund, R.; Zaremba, O.; Arnauts, G.; Ameloot, R.; Skorupskii, G.; Dincă, M.; Bavykina, A.; Gascon, J.; Ejsmont, A.; Goscianska, J. et al. The current status of MOF and COF applications. *Angew. Chem., Int. Ed.* **2021**, *60*, 23975–24001.
[21] Liu, F.; Lin, L.; Zhang, Y.; Wang, Y. B.; Sheng, S.; Xu, C. N.; Tian, H. Y.; Chen, X. S. A tumor-microenvironment-activated nanozyme-mediated theranostic nanoreactor for imaging-guided combined tumor therapy. *Adv. Mater.* **2019**, *31*, 1902885.
[22] Li, Z. L.; Lai, X. Q.; Fu, S. Q.; Ren, L.; Cai, H.; Zhang, H.; Gu, Z. W.; Ma, X. L.; Luo, K. Immunogenic cell death activates the tumor immune microenvironment to boost the immunotherapy efficiency. *Adv. Sci.* **2022**, *9*, 2201734.
[23] Wang, S. Z.; Guo, Y. X.; Zhang, X. P.; Feng, H. H.; Wu, S. Y.; Zhu, Y. X.; Jia, H. R.; Duan, Q. Y.; Hao, S. J.; Wu, F. G. Mitochondria-targeted photodynamic and mild-temperature photothermal therapy for realizing enhanced immunogenic cancer cell death via mitochondrial stress. *Adv. Funct. Mater.* **2023**, *33*, 2303328.
[24] Banstola, A.; Poudel, K.; Kim, J. O.; Jeong, J. H.; Yook, S. Recent progress in stimuli-responsive nanosystems for inducing immunogenic cell death. *J. Control. Release* **2021**, *337*, 505–520.
[25] Li, S. K.; Zhang, W. J.; Xing, R. R.; Yuan, C. Q.; Xue, H. D.; Yan, X. H. Supramolecular nanofibrils formed by coassembly of clinically approved drugs for tumor photothermal immunotherapy. *Adv. Mater.* **2021**, *33*, 2100595.
[26] Wang, M.; Zhang, X. H.; Liu, B.; Liu, C.; Song, C. M.; Chen, Y.; Jin, Y. B.; Lin, J.; Huang, P.; Xing, S. J. Immunotherapeutic hydrogel with photothermal induced immunogenic cell death and STING activation for post-surgical treatment. *Adv. Funct. Mater.* **2023**, *33*, 2300199.
[27] Ou, W. Q.; Stewart, S.; White, A.; Kwizera, E. A.; Xu, J. S.; Fang, Y. Z.; Shamul, J. G.; Xie, C. Q.; Nurudeen, S.; Tirada, N. P. et al. *In situ* cryo-immune engineering of tumor microenvironment with cold-responsive nanotechnology for cancer immunotherapy. *Nat. Commun.* **2023**, *14*, 392.
[28] Lv, Y. L.; Li, F.; Wang, S.; Lu, G. H.; Bao, W. E.; Wang, Y. G.; Tian, Z. Y.; Wei, W.; Ma, G. H. Near-infrared light-triggered platelet arsenal for combined photothermal-immunotherapy against cancer. *Sci. Adv.* **2021**, *7*, eabd7614.
[29] Li, W.; Yang, J.; Luo, L. H.; Jiang, M. S.; Qin, B.; Yin, H.; Zhu, C. Q.; Yuan, X. L.; Zhang, J. L.; Luo, Z. Y. et al. Targeting photodynamic and photothermal therapy to the endoplasmic reticulum enhances immunogenic cancer cell death. *Nat. Commun.* **2019**, *10*, 3349.
[30] Deng, Z.; Liu, J. W.; Xi, M.; Wang, C. J.; Fang, H. P.; Wu, X. R.; Zhang, C.; Sun, G. T.; Zhang, Y. F.; Shen, L. et al. Biogenic platinum nanoparticles on bacterial fragments for enhanced radiotherapy to boost antitumor immunity. *Nano Today* **2022**, *47*, 101656.
[31] Xu, Y.; Guo, Y. Q.; Zhang, C. C.; Zhan, M. S.; Jia, L.; Song, S. L.; Jiang, C. J.; Shen, M. W.; Shi, X. Y. Fibronectin-coated metal-phenolic networks for cooperative tumor chemo-/chemodynamic/immune therapy via enhanced ferroptosis-mediated immunogenic cell death. *ACS Nano* **2022**, *16*, 984–996.
[32] Yang, W. J.; Zhang, F. W.; Deng, H. Z.; Lin, L. S.; Wang, S.; Kang, F.; Yu, G. C.; Lau, J.; Tian, R.; Zhang, M. R. et al. Smart nanovesicle-mediated immunogenic cell death through tumor microenvironment modulation for effective photodynamic immunotherapy. *ACS Nano* **2020**, *14*, 620–631.
[33] Yang, C. Z.; Wang, M.; Chang, M. Y.; Yuan, M.; Zhang, W. Y.; Tan, J.; Ding, B. B.; Ma, P. A.; Lin, J. Heterostructural nanoadjuvant CuSe/$CoSe_2$ for potentiating ferroptosis and photoimmunotherapy through intratumoral blocked lactate efflux. *J. Am. Chem. Soc.* **2023**, *145*, 7205–7217.
[34] Zhang, J.; Pan, Y. W.; Liu, L. J.; Xu, Y. T.; Zhao, C. C.; Liu, W.; Rao, L. Genetically edited cascade nanozymes for cancer immunotherapy. *ACS Nano* **2024**, *18*, 12295–12310.
[35] Luo, T. K.; Fan, Y. J.; Mao, J. M.; Yuan, E.; You, E.; Xu, Z. W.; Lin, W. B. Dimensional reduction enhances photodynamic therapy of metal-organic nanophotosensitizers. *J. Am. Chem. Soc.* **2022**, *144*, 5241–5246.
[36] Li, Z.; Chu, Z. Y.; Yang, J.; Qian, H. S.; Xu, J. M.; Chen, B. J.; Tian, T.; Chen, H.; Xu, Y. S.; Wang, F. Immunogenic cell death augmented by manganese zinc sulfide nanoparticles for metastatic melanoma immunotherapy. *ACS Nano* **2022**, *16*, 15471–15483.
[37] Xu, W. X.; Li, D. D.; Chen, C. R.; Wang, J. X.; Wei, X. H.; Yang, X. Z. Design of mitoxantrone-loaded biomimetic nanocarrier with sequential photothermal/photodynamic/chemotherapy effect for synergized immunotherapy. *Adv. Funct. Mater.* **2023**, *33*, 2302231.
[38] Liu, X. Y.; Zhuang, Y. P.; Huang, W.; Wu, Z. Z.; Chen, Y. J.; Shan, Q. G.; Zhang, Y. F.; Wu, Z. Y.; Ding, X. Y.; Qiu, Z. L. et al. Interventional hydrogel microsphere vaccine as an immune amplifier for activated antitumour immunity after ablation therapy. *Nat. Commun.* **2023**, *14*, 4106.
[39] Yang, K.; Qi, S. L.; Yu, X. Y.; Bai, B.; Zhang, X. Y.; Mao, Z. W.; Huang, F. H.; Yu, G. C. A hybrid supramolecular polymeric nanomedicine for cascade-amplified synergetic cancer therapy. *Angew. Chem., Int. Ed.* **2022**, *61*, e202203786.

[40] Wu, W. C.; Pu, Y. Y.; Zhou, B. G.; Shen, Y. C.; Gao, S.; Zhou, M.; Shi, J. L. Photoactivatable immunostimulatory nanomedicine for immunometabolic cancer therapy. *J. Am. Chem. Soc.* **2022**, *144*, 19038–19050.

[41] Sun, M. Y.; Liu, Z. W.; Wu, L.; Yang, J.; Ren, J. S.; Qu, X. G. Bioorthogonal-activated *in situ* vaccine mediated by a COF-based catalytic platform for potent cancer immunotherapy. *J. Am. Chem. Soc.* **2023**, *145*, 5330–5341.

[42] Duan, X. P.; Chan, C.; Han, W. B.; Guo, N. N.; Weichselbaum, R. R.; Lin, W. B. Immunostimulatory nanomedicines synergize with checkpoint blockade immunotherapy to eradicate colorectal tumors. *Nat. Commun.* **2019**, *10*, 1899.

[43] Zhou, Y.; Zhang, Y. W.; Jiang, C. Q.; Chen, Y. X.; Tong, F.; Yang, X. T.; Wang, Y. Z.; Xia, X.; Gao, H. L. Rosmarinic acid-crosslinked supramolecular nanoassembly with self-regulated photodynamic and anti-metastasis properties for synergistic photoimmunotherapy. *Small* **2023**, *19*, 2300594.

[44] Yu, L.; Yu, M.; Chen, W.; Sun, S. J.; Huang, W. X.; Wang, T. Q.; Peng, Z. W.; Luo, Z. W.; Fang, Y. X.; Li, Y. J. et al. *In situ* separable nanovaccines with stealthy bioadhesive capability for durable cancer immunotherapy. *J. Am. Chem. Soc.* **2023**, *145*, 8375–8388.

[45] Liu, F.; Lin, L.; Zhang, Y.; Sheng, S.; Wang, Y. B.; Xu, C. N.; Tian, H. Y.; Chen, X. S. Two-dimensional nanosheets with high curcumin loading content for multimodal imaging-guided combined chemo-photothermal therapy. *Biomaterials* **2019**, *223*, 119470.

[46] Zhong, Y. L.; Li, T. Y.; Zhu, Y. F.; Zhou, J.; Akinade, T. O.; Lee, J.; Liu, F.; Bhansali, D.; Lao, Y. H.; Quek, C. H. et al. Targeting proinflammatory molecules using multifunctional MnO nanoparticles to inhibit breast cancer recurrence and metastasis. *ACS Nano* **2022**, *16*, 20430–20444.

[47] Fadus, M. C.; Lau, C.; Bikhchandani, J.; Lynch, H. T. Curcumin: An age-old anti-inflammatory and anti-neoplastic agent. *J. Tradit. Complement. Med.* **2017**, *7*, 339–346.

[48] Jeon, M.; Halbert, M. V.; Stephen, Z. R.; Zhang, M. Q. Iron oxide nanoparticles as T_1 contrast agents for magnetic resonance imaging: Fundamentals, challenges, applications, and prospectives. *Adv. Mater.* **2021**, *33*, 1906539.

[49] Rezaei, B.; Yari, P.; Sanders, S. M.; Wang, H. T.; Chugh, V. K.; Liang, S.; Mostufa, S.; Xu, K. L.; Wang, J. P.; Gómez-Pastora, J. et al. Magnetic nanoparticles: A review on synthesis, characterization, functionalization, and biomedical applications. *Small* **2024**, *20*, 2304848.

[50] Chang, R.; Zou, Q. L.; Zhao, L. Y.; Liu, Y. M.; Xing, R. R.; Yan, X. H. Amino-acid-encoded supramolecular photothermal nanomedicine for enhanced cancer therapy. *Adv. Mater.* **2022**, *34*, 2200139.

[51] Hao, J, N.; Ge, K. M.; Chen, G. L.; Dai, B.; Li, Y. S. Strategies to engineer various nanocarrier-based hybrid catalysts for enhanced chemodynamic cancer therapy. *Chem. Soc. Rev.* **2023**, *52*, 7707–7736.

[52] Zou, Q. L.; Abbas, M.; Zhao, L. Y.; Li, S. K.; Shen, G. Z.; Yan, X. H. Biological photothermal nanodots based on self-assembly of peptide-porphyrin conjugates for antitumor therapy. *J. Am. Chem. Soc.* **2017**, *139*, 1921–1927.

[53] Guo, Y. X.; Wang, S. Z.; Zhang, X. P.; Jia, H. R.; Zhu, Y. X.; Zhang, X. D.; Gao, G.; Jiang, Y. W.; Li, C. C.; Chen, X. K. et al. *In situ* generation of micrometer-sized tumor cell-derived vesicles as autologous cancer vaccines for boosting systemic immune responses. *Nat. Commun.* **2022**, *13*, 6534.

[54] Yu, J. F.; Zhou, B. G.; Zhang, S.; Yin, H. H.; Sun, L. P.; Pu, Y. Y.; Zhou, B. Y.; Sun, Y. K.; Li, X. L.; Fang, Y. et al. Design of a self-driven probiotic-CRISPR/Cas9 nanosystem for sono-immunometabolic cancer therapy. *Nat. Commun.* **2022**, *13*, 7903.

[55] Qiao, G. X.; Li, S. L.; Pan, X. M.; Xie, P.; Peng, R. X.; Huang, X. R.; He, M. Y.; Jiang, J. H.; Chu, X. Surgical tumor-derived nanoplatform targets tumor-associated macrophage for personalized postsurgical cancer immunotherapy. *Sci. Adv.* **2024**, *10*, eadk7955.

[56] Ren, L.; Lim, Y. T. Degradation-regulatable architectured implantable macroporous scaffold for the spatiotemporal modulation of immunosuppressive microenvironment and enhanced combination cancer immunotherapy. *Adv. Funct. Mater.* **2018**, *28*, 1804490.

[57] Steenbrugge, J.; Bellemans, J.; Elst, N. V.; Demeyere, K.; de Vliegher, J.; Perera, T.; de Wever, O.; van den Broeck, W.; de Spiegelaere, W.; Sanders, N. N. et al. One cisplatin dose provides durable stimulation of anti-tumor immunity and alleviates anti-PD-1 resistance in an intraductal model for triple-negative breast cancer. *OncoImmunology* **2022**, *11*, 2103277.

[58] Liu, X. L.; Chen, Y. J.; Fu, Y.; Jiang, D. X.; Gao, F. Y.; Tang, Z. J.; Bian, X. F.; Wu, S.; Yu, Y.; Wang, X. Y. et al. Breaking spatiotemporal barriers of immunogenic chemotherapy via an endoplasmic reticulum membrane-assisted liposomal drug delivery. *ACS Nano* **2023**, *17*, 10521–10534.

[59] Gao, C.; Wang, Q. F.; Li, J. Y.; Kwong, C. H. T.; Wei, J. W.; Xie, B. B.; Lu, S. Y.; Lee, S. M. Y.; Wang, R. B. *In vivo* hitchhiking of immune cells by intracellular self-assembly of bacteria-mimetic nanomedicine for targeted therapy of melanoma. *Sci. Adv.* **2022**, *8*, eabn1805.

[60] Wang, Y.; Gao, D.; Jin, L.; Ren, X. C.; Ouyang, Y. A.; Zhou, Y.; He, X. Y.; Jia, L. L.; Tian, Z. M.; Wu, D. C. et al. NADPH selective depletion nanomedicine-mediated radio-immunometabolism regulation for strengthening Anti-PDL1 therapy against TNBC. *Adv. Sci.* **2023**, *10*, 2203788.

[61] Liu, D.; Liang, S.; Ma, K. S.; Meng, Q. F.; Li, X. G.; Wei, J.; Zhou, M. L.; Yun, K. Q.; Pan, Y. W.; Rao, L. et al. Tumor microenvironment-responsive nanoparticles amplifying STING signaling pathway for cancer immunotherapy. *Adv. Mater.* **2024**, *36*, 2304845.

[62] Haabeth, O. A. W.; Blake, T. R.; McKinlay, C. J.; Tveita, A. A.; Sallets, A.; Waymouth, R. M.; Wender, P. A.; Levy, R. Local delivery of *OX40L*, *CD80*, and *CD86* mRNA kindles global anticancer immunity. *Cancer Res.* **2019**, *79*, 1624–1634.

[63] Tekguc, M.; Wing, J. B.; Osaki, M.; Long, J.; Sakaguchi, S. Treg-expressed CTLA-4 depletes CD80/CD86 by trogocytosis, releasing free PD-L1 on antigen-presenting cells. *Proc. Natl. Acad. Sci. USA* **2021**, *118*, e2023739118.

[64] Jiang, Y.; Krishnan, N.; Zhou, J. R.; Chekuri, S.; Wei, X. L.; Kroll, A. V.; Yu, C. L.; Duan, Y. O.; Gao, W. W.; Fang, R. H. et al. Engineered cell-membrane-coated nanoparticles directly present tumor antigens to promote anticancer immunity. *Adv. Mater.* **2020**, *32*, 2001808.

[65] Yong, S. B.; Chung, J. Y.; Song, Y.; Kim, J.; Ra, S.; Kim, Y. H. Non-viral nano-immunotherapeutics targeting tumor microenvironmental immune cells. *Biomaterials* **2019**, *219*, 119401.